Hindawi
Advances in Materials Science and Engineering
Volume 2019, Article ID 3726953, 18 pages
https://doi.org/10.1155/2019/3726953

Research Article

Pore Structure Characterization of Hardened Cement Paste by Multiple Methods

Yang Song, Jun-wen Zhou, Zheng-ning Bian, and Guo-zhong Dai

School of Civil Engineering & Architecture, Changzhou Institute of Technology, Changzhou 213032, China

Correspondence should be addressed to Yang Song; songy@czu.cn

Received 14 July 2019; Revised 18 October 2019; Accepted 1 November 2019; Published 12 December 2019

Academic Editor: Barbara Liguori

Pore structure characterization of hardened cement paste is important to concrete mechanical and transport properties. Hence, we apply indirect methods (NS, MIP, and NMR) and direct methods (XCT, FIB/SEM, and HIM) to provide a general view of the pore structure of hardened cement paste. The results show that the 3D pore network of hardened cement paste is isolated in microscale yet is largely connected by large capillary pores, small capillary pores, and microcracks in nanoscale. In indirect methods, MIP and NMR have a wide measurement range and permit observing most of the porous volume with an average porosity of 8.4–9.9% of hardened cement paste. In contrast, direct methods have a relatively narrow measurement range and thus lead to a large porosity scattering of 1.8–16.4%. The pore size distribution (PSD) curves by indirect methods show that the pore structure is mainly concentrated in three sections of 1–10 nm, 10–100 nm, and around 10 μm, which correspond to the imaging range of HIM, FIB/SEM, and XCT. However, FIB/SEM implies that the most porous part of hardened cement paste (10–100 nm) is underestimated by MIP due to the "ink-bottle" effect. Another "underestimation" of NMR is because C-S-H gels swell during the wetting, and the swelling separates the capillary pores into smaller ones. The microcracks induced by sample preparation contribute 0.1-0.2% (XCT) and 4.5–8.1% (FIB/SEM) of porosity to the porous volume of cement paste, but they have limited influence on the pore size distribution and pore connectivity.

1. Introduction

Concrete is a commonly used civil engineering material with multiscale and multicomponent porous volume. Among the components of concrete, hardened cement paste contains the largest part of porous volume and thus plays an important role in concrete mechanical and transport properties. Literature studies show that transport properties, including diffusion and permeation, are directly related to porosity, pore size, connectivity, and tortuosity of cement paste [1, 2]. And the harmful matter, such as SO_4^{-2}, O_2, and Cl^{-1}, also mainly passes through the pore network into the inner volume. Thus, to better understand the concrete properties, we need to characterize the pore morphology of hardened cement paste.

The pore structure of hardened cement paste is multiscale and multicomponent. Previous literature studies devise the pore structure of hardened cement paste into four parts: gel pores (<10 nm), small capillary pores (10–100 nm), large capillary pores (100–1000 nm), and air holes (>several μm) [3]. In fact, many methods have been applied to characterize the pore structure of hardened cement paste or concrete. Nitrogen adsorption (NS) is based on the molecule adsorption of porous volume and is used to detect the smallest volume, gel pores (<10 nm), of cement paste. Mercury intrusion porosimetry (MIP) permits detecting pores from 5 nm to several microns [4–6]. Yio et al. [3] apply MIP to the blended cementitious materials and obtain a porosity of 10–30%. The measured pore size distribution (PSD) varies from 3 nm to 10 μm and mainly focuses on the range of 10–200 nm. In fact, the PSD obtained by MIP is preferred to be "pore entry size distribution" because MIP is based on the relation between mercury pressure and its intrusion volume. The "ink-bottle" effect leads to underestimating the pore size of hardened cement paste. In addition, the results of MIP are also sensitive to the mercury contact angle and surface tension, which can hardly be accurately measured. In contrast, nuclear magnetic resonance (NMR) is applied to water-

saturated cement paste samples and thus permits detecting the porous volume in the saturated state [7]. Since water wetting swells the C-S-H gel, the pore structure of C-S-H varies a lot and the pore size turns to be at least one time smaller than before [8]. Although the above methods provide porosity and PSD curves of hardened cement paste, they cannot directly observe the porous volume and characterize the pore structure of cement paste.

In contrast, direct methods, such as X-ray computed tomography (XCT), laser scanning confocal microscopy (LSCM), and scanning electron microscopy (SEM), permit directly characterizing the pore structure by image analysis. XCT has been applied to investigate the 3D pore network of concrete and hardened cement paste [9, 10]. Due to the resolution limit, XCT only permits observing the pore network in microns, which belongs to microcracks and air holes. Thus, XCT is relatively applicable to observe the pore structure of cement paste in the early age [3, 9]. LSCM is another method for characterizing the 3D pore structure of cementitious materials, but with finer resolution (down to around 0.2 μm) than XCT [11]. Because of submicron resolution, LSCM can capture large capillary pores in cement paste, where the 3D connected porous volume is partially connected and thus provides a first view of tortuosity and connectivity of hardened cement paste [11]. Despite this, LSCM still does not permit giving a general view of capillary pores in hydrated cement paste. SEM can observe images with resolution down to around 3 nm and thus is applied to characterize the pore morphology of capillary pores in hardened cement paste [12]. Based on the SEM images, one can analyse porosity, PSD, pore shape, and representative elementary area (REA) of porous volume, which helps to understand the material transport in porous volume of hardened cement paste [13]. However, SEM can only scan the sample's surface, while the inner porous volume is still largely unknown. Focused ion beam/scanning electron microscopy (FIB/SEM) permits researching the 3D porous volume at the same scale of SEM [1, 14]. With 3D porous volume, the 3D pore morphology, pore network tortuosity, and pore connectivity, which are key parameters to understand the fluid transport in hardened cement paste, can be analysed. To date, few researchers have applied this method to observe the 3D porous volume of cement-based materials [1, 14]. For finer observation, transmission electron microscopy (TEM) can observe the gel pores with the resolution down to less than 1 nm [1, 13]. Previous literature studies show that TEM images provide a similar pore width distribution with the dominant pore size of around 5 nm, which is similar to the results of argon adsorption [15]. However, it is challenging for TEM to cut samples into slices of dozens of nanometres thick to obtain the high resolution [16]. In contrast, helium ion microscopy (HIM) is a method which permits observing gel pores and provides image resolution down to around 1.0 nm. It does not need specific preparation as TEM and can be easily applied as SEM. At present, HIM has not been used for cement-based materials.

Although considerable research has analysed the 2D porous volume of hardened cement paste and gives a first view of macropores in 3D, the 3D pore network, especially the capillary pores, of hardened cement paste is still largely unknown. Furthermore, few studies have adequately explored the porous volume of hardened cement paste regarding the suitability of different methods (both indirect methods and direct methods) for characterizing the pore structure of hardened cement paste. Therefore, for a better understanding of porous volume, we apply the indirect methods, e.g., NS, MIP, and NMR, and the direct methods, e.g., XCT, FIB/SEM, and HIM, to characterize the pore structure of hardened cement paste. Then, the porosity, pore surface area, PSD, and pore connectivity are listed, compared, and further discussed.

2. Materials

This research aims to provide a general view of the multiscale and multicomposition pore network of hardened cement paste by multiple methods. Thus, the common mixture of C40 concrete is applied in the test, and the mix design of concrete is listed in Table 1. The mixture of cement paste is poured into a cube of 150 mm^3 and is cured at the standard condition ($T = 20^\circ$C, $RH = 100\%$) for 90 days. Its compressive strength is measured to be 42.1 ± 0.7 MPa at the age of 28 days. Since this research focuses on the porous volume in hardened cement paste, gains of cement paste are stripped of concrete manually and then applied to the following tests. This induces damages to the observed samples and leads to uncertain proportion of cement paste, which are discussed in Results and Discussion.

3. Experimental Methods

3.1. Indirect Methods

3.1.1. Nitrogen Adsorption. Nitrogen adsorption is a commonly used method to capture the pore properties of the cementitious material. It measures the adsorbed nitrogen with varying nitrogen pressure in the form of the adsorption isotherm at 77 K. Then, based on the adsorption curve, we can obtain the specific surface area (SSA) and PSD based on the 8-point Brunauer–Emmett–Teller (BET) theory and BJH (Barrett–Joyner–Halenda) model. The relationship between pore size and relative pressure is based on the Kelvin equation:

$$\ln\left(\frac{P_v}{P_{\text{sat}}}\right) = \frac{-2 \cdot H \cdot \gamma \cdot V_l}{R \cdot T}, \tag{1}$$

where P_v is the equilibrium vapour pressure, P_{sat} is the saturation vapour pressure, H is the mean curvature of the meniscus, γ is the liquid/vapour surface tension, V_l is the liquid molar volume, R is the ideal gas constant, and T is the temperature.

Before the NS test, cement paste gains are stripped from the concrete sample and are then oven-dried at 65°C until mass stabilization. Three particles (NS1, NS2, and NS3) of hardened cement paste are applied to the test, and the information on samples is listed in Table 2. Nitrogen adsorption is carried out on Micromeritics ASAP 2010 with the nitrogen pressure ranging up to 126.66 kPa. And the relative

Table 1: Concrete mix design.

Content of fly ash (%)	Water-binder ratio	Cement P.O.42.5 (kg/m^3)	Fly ash (kg/m^3)	Sand (kg/m^3)	Stone (kg/m^3)	Water (kg/m^3)
30	0.45	280	120	638	1182	180

Table 2: Samples applied to multiple methods.

Methods		Samples	Test range	Mass (g)	Voxel/pixel size	Sample volume
Indirect method	Nitrogen sorption	NS1	2 nm to 60 nm	1.21		
		NS2		0.88		
		NS3		0.43		
	MIP	MIP1	5.1 nm to dozens of microns	1.29		
		MIP2		1.35		
		MIP3		2.00		
		MIP4		1.11		
	Nuclear magnetic resonance	NMR1	1 nm to dozens of microns	69.23		
		NMR2		5.42		
Direct method	X-ray tomography	XCT1	1 μm to hundreds of microns		$1.0 \times 1.0 \times 1.0\ \mu m^3$	$1.0 \times 1.0 \times 1.0\ mm^3$
		XCT2			$1.0 \times 1.0 \times 1.0\ \mu m^3$	$1.0 \times 1.0 \times 1.0\ mm^3$
	FIB/SEM	FS1	10 nm to several microns		$10 \times 10 \times 20\ nm^3$	$6.85 \times 8.80 \times 8.08\ \mu m^3$
		FS2			$10 \times 10 \times 20\ nm^3$	$9.61 \times 6.16 \times 7.78\ \mu m^3$
	Helium ion microscopy	H1	1 nm to several microns		$1.0 \times 1.0\ nm^2$	$8.0 \times 8.0\ \mu m^2$
		H2			$1.0 \times 1.0\ nm^2$	$8.0 \times 8.0\ \mu m^2$

pressure P/P_0 range for Langmuir/BET evaluation is 0.05–0.35, whereas the P/P_0 range for BJH evaluation is 0.4–0.967.

3.1.2. Mercury Intrusion Microscopy. Four particles (M1, M2, M3, and M4) of hardened cement paste are prepared and dried in an oven at 65°C until weight stabilization. Then, the MIP test is applied by Micromeritics® AutoPore IV 9510 with the following parameters: the contact angle is 130°, the surface tension is 485.000 dynes/cm, and the Hg pressure is up to 413.7 MPa. The relationship between pore size and mercury pressure is governed by the Washburn–Laplace equation, based on the assumption of cylindrical capillary:

$$d = \frac{P}{4\gamma \cos\theta}, \tag{2}$$

where d is the pore access diameter, P is the mercury injection pressure, γ is the surface tension of mercury, and θ is the contact angle between solid and mercury. The information on three samples for MIP is presented in Table 2.

3.1.3. Nuclear Magnetic Resonance. Nuclear magnetic resonance is used to analyse the transverse relaxation time T_2 of a return to equilibrium, in response to a magnetic disturbance [7]. The relaxation time T_2 depends mainly on the surface (S) and pore volume (V), and the relaxivity of the surface (ρ) [17]. The standard interpretation is based on the relationship of the time T_2:

$$\frac{1}{T_2} = \rho \frac{S}{V}. \tag{3}$$

To calculate the diameter d of cylindrical pores, the ratio S/V is equal to $1/d$. In addition, the conversion of relaxation time in the pore sizes requires a calibration value of relaxivity of the surface (ρ). In this research, two cement paste samples (NMR1 and NMR2) are water saturated in a desiccator under vacuum until the weight stays constant. NMR experiments are performed using a MesoMR23-060H-I medium-sized NMR analyser (Suzhou Niumag Analytical Instrument Corporation) with a resonance frequency of 21 MHz. The echo time TE is 0.2 ms, the waiting time TW is 4500 ms, and the cumulative adoption times NS is 16. According to previous research, the relaxivity of the surface ρ for water is yielded as 1.89 m/s [8]. Then based on equation (3), we convert the relaxation times to the pore size, and the pore size distribution can be obtained. After the NMR experiment, the samples are oven-dried at 65°C until mass stabilization. Then, the porosity by mass weighting can be obtained and compared with that of NMR analysis.

3.2. Direct Methods

3.2.1. X-Ray Tomography. Cylinders of hardened cement paste applied to XCT observation are drilled from one large concrete block that is 2.0 mm in height and 1.5 mm in diameter (Table 2). Then, the drilled samples are oven-dried at 65°C until mass stabilization, attached to the base of observation, and put into Xradia 520 Versa 3D.

After XCT scanning, the raw images are filtered to remove the "ring" and "pepper-salt" noises in ImageJ. Then, we apply the plugin "Multi-OTSU algorithm" in ImageJ to segment the porous volume and small aggregates [18]. To view the images in 3D, we rebuild the 3D volume of raw images with "SurfaceGen" in Avizo software and then illustrate its porous volume of hardened cement paste in 3D (Figure 1). The porosity and PSD are obtained by the continuous pore size distribution method, which is detailed in previous literature studies [1, 19].

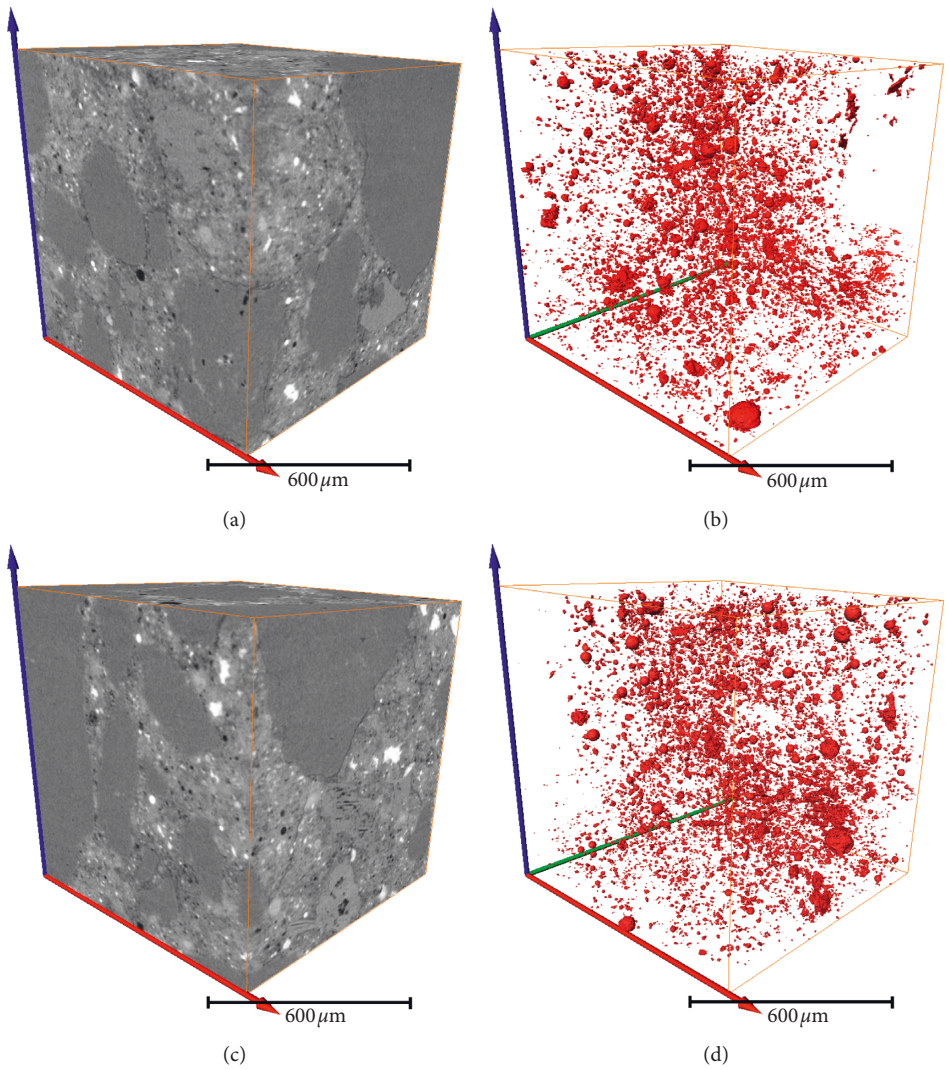

Figure 1: Raw images and segmented porous volume of hardened cement paste by XCT.

3.2.2. FIB/SEM. For imaging preparation of FIB/SEM, the aimed sample is taken from the concrete cube and is cut into a slice of 2–5 mm height with the aimed area of hardened cement paste. Then, the slice is oven-dried at 65°C until mass stabilization. To facilitate the observation, the two surfaces of the sample are roughly polished by sandpaper and finely argon ion polished by Leica EM TIC 3X. The polished surface is metal sprayed to enhance the electrical conductivity of the concrete surface. Then, the sample is sent to Zeiss Crossbeam 540 for selecting the objected zone in the 2D mode (Figure 2(a)). After selecting the aimed zone, the concave area around the selected zone is removed by FIB and the cross section of aimed volume is well prepared (Figure 2(b)). Finally, the FIB and SEM work alternatively, and the image stacks of hardened cement paste are obtained.

To analyse the porous volume, several steps of image processing are performed using the software Image J. First revise is applied to lengthen the height of images with a ratio of 1/sin 54°, for samples are tilted at 54° aiming to imaging their cross section. The tilted images are realigned to adjust the displacement occurring during the slicing procedure, and the maximal overlapping area is cropped for image analysis. Then, the cropped images are filtered by the background filter, FFT filter, and "Median 3D" filter to remove the shadow effect, water curtain effect, and "salt and pepper" noises, respectively. Finally, the FIB/SEM images are segmented by the Otsu algorithm because of its stable segmentation effect [20–22]. Details of image filtration and segmentation of FIB/SEM images are also presented in previous literature studies [20–22]. Information on cement paste specimens is shown in Table 2, and the 3D structures of concrete are reconstructed by "SurfaceGen" in Avizo software (Figure 3). The porosity and PSD of porous volume of hardened cement paste are also obtained by the continuous pore size distribution method.

3.2.3. Helium Ion Microscopy. Helium ion microscopy (HIM) utilizes a helium beam with a spot diameter of 0.4 nm for scanning the sample surface and thus provides a much higher resolution than SEM [23]. Before HIM observation, the aimed cement paste is cut into cubes of

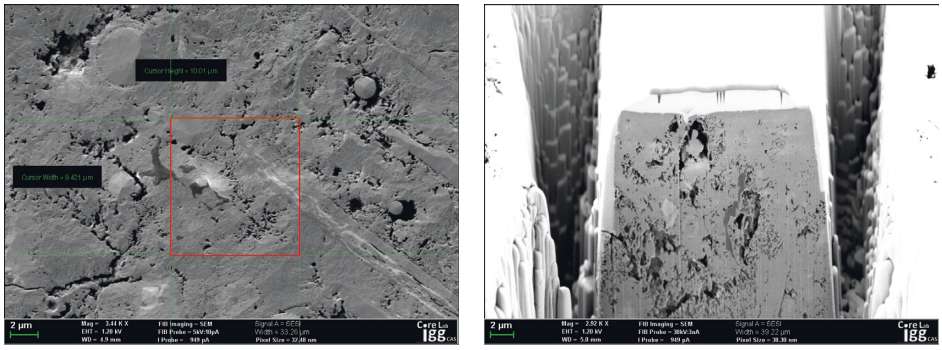

(a) (b)

Figure 2: Process of FIB/SEM imaging: (a) aimed surface in 2D SEM; (b) cropped cross section of cement paste.

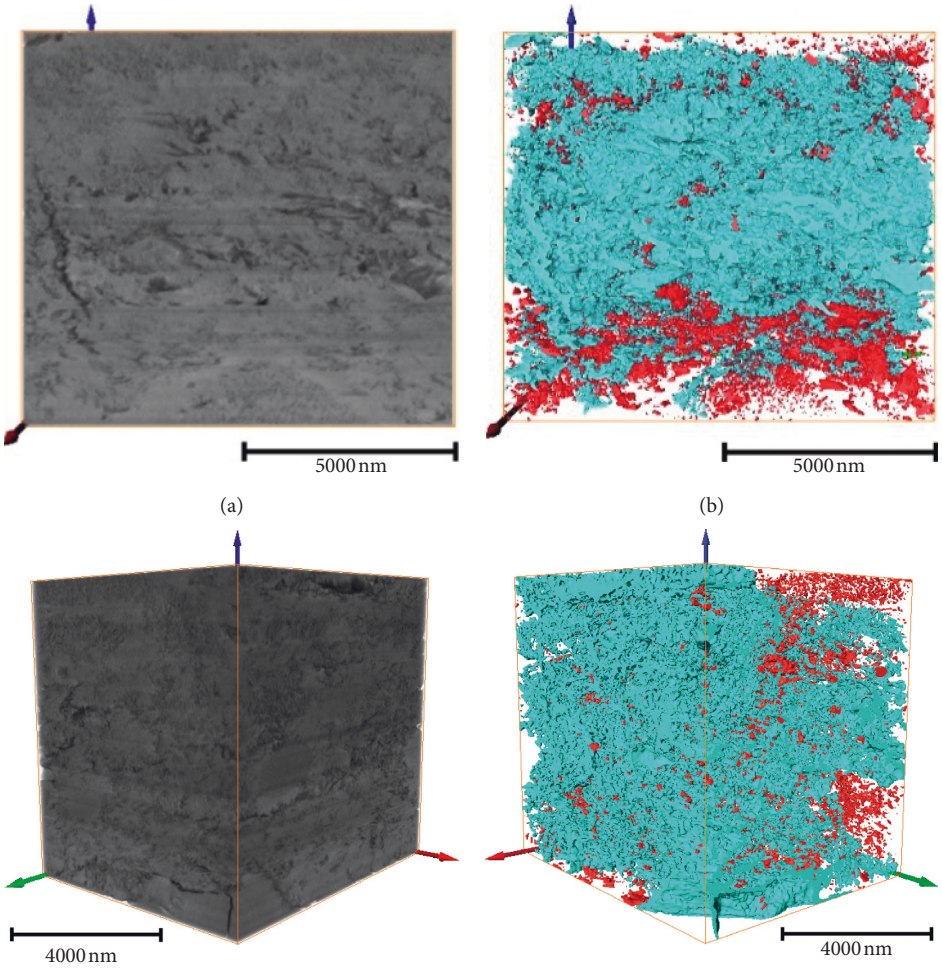

(a) (b)

(c) (d)

Figure 3: Continued.

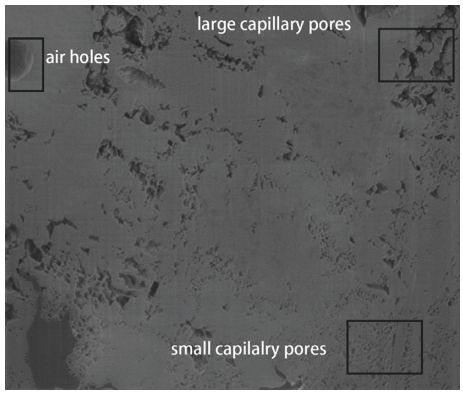

(e)

Figure 3: Raw images and segmented porous volume of hardened cement paste by FIB/SEM: (a) original images of FS1; (b) segmented porous volume of FS1; (c) original images of FS2; (d) segmented porous volume of FS2; (e) 2D image by FIB/SEM.

$0.5 \times 0.5 \times 0.5\ \text{cm}^3$. Then, the sample surface is polished as FIB/SEM samples. The surface of the cement paste sample is metal sprayed to enhance the electrical conductivity. HIM observation is conducted by a ZEISS Orion Plus microscope with parameters of observations as follows: the beam accelerating voltage is 30 kV and the beam current is 0.422 PA with the vacuum of 5×10^{-7} Torr.

After observation, the HIM images are filtered by the "median" filter to remove the "pepper and salt" noises. Then, the images are segmented by the Otsu algorithm.

4. Results and Discussion

4.1. Pore Morphology. The isotherm sorption of hardened cement paste by NS is presented in Figure 4. The three curves show similar forms and all begin with a flat direct line from a relative pressure of 0.05 to 0.8. Then, they augment sharply from a relative pressure of 0.8 to 1.0. During desorption, the curves form a narrow hysterics loop during a relative pressure of 1.0 to 0.45, which is due to condensation. Then, the curves drop sharply and overlap with the sorption curves. Compared with traditional forms, the curves correspond to Isotherm Sorption Curve IV and Hysteresis Loop III [2, 24]. This implies that the pore network of hardened cement paste is mainly composed of micropores and mesopores, and the porous volume is mostly a slice-like form, which is similar to clay minerals [25].

As a direct method, XCT captures a large amount of ball-shaped pores and several microcracks all around the hardened cement paste volume (Figure 1). Most of these pores are air holes and mainly generated during the concrete pouring. Due to the resolution limit, XCT cannot observe pores less than 1 μm, and thus, the gel pores and capillary pores are not detected.

In contrast, FIB/SEM reduces the observing scale and permits detecting 3D porous volume down to 10 nm. In Figure 3, raw images and the segmented porous volumes illustrate that the porous volumes are largely connected in the form of capillary instead of slice. This is opposite to the results of NS, which implies that the indirect method may induce misunderstanding the pore morphology of hardened

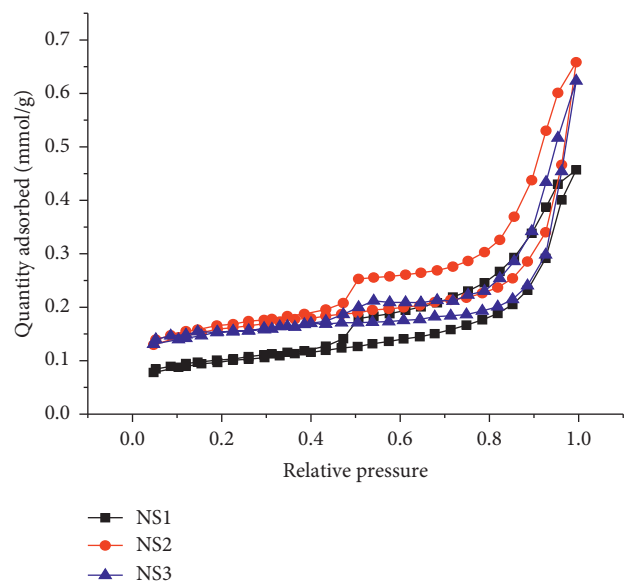

Figure 4: Isotherm sorption of hardened cement paste by nitrogen adsorption.

cement paste. As presented in previous literature [1, 14], four series of porous volumes are observed in FIB/SEM images (Figure 3(e)): air holes, microcracks, large capillary pores, and small capillary pores [8, 13]. 3D images show that the porous volume is largely connected by large capillary pores and small capillary pores. Meanwhile, a small part of small capillary pores is observed to be isolated. This agrees with other research where the hydrated cement particles are separated into the dense cluster and loose cluster [14]. The dense cluster has smaller porosity and less connected porous volume than the loose cluster, whereas in the loose cluster, the hydrated cement particles are much more porous and largely connected.

In HIM images, the gel pores (smaller than 10 nm) are located around capillary pores and seem to be connected with capillary pores in inner volume (Figure 3). However, the porous volume in HIM images is not surface connected in 2D, which is the opposite to the results of other research

[15]. This is because the connectivity of gel pores can hardly be observed in 2D images. Moreover, certain gel pores are covered by metal spraying during the sample preparation and cannot be observed, which also limits the connectivity of gel pores.

4.2. Porosity and Pore Surface Area. Porosity and pore surface area are important properties of the porous medium. The porosity and pore surface area obtained by multiple methods are listed in Table 3.

4.2.1. Porosity by Indirect Methods. The indirect methods have a relatively wide measurement range and can detect most of porous volume in hardened cement paste (Table 3). Among the indirect methods, MIP provides the largest average porosity of 9.9% and the pore size ranges from gel pores to macropores focusing on the capillary pores (Table 3). NMR is another method which permits observing all the porous volume, and it gives an average porosity of 8.4%. Compared with MIP, NMR is more focused on gel pores (49.7% of porosity) instead of small capillary pores (37.3% of porosity). In contrast, MIP is just the opposite with 1.0% of porosity for gel pores and 69.3% of porosity for small capillary pores. This difference is partly because the NMR permits detecting the gel pores, which is out of observation of the other methods. This is also partly because the wetting of hardened cement paste induces swelling of C-S-H gels and the capillary pores turn to be gel pores [8]. It can be verified that MIP (porous volume of 7.3%) and NMR (porous volume of 7.2%) provide similar porous volumes by adding gel pores and small capillary pores. NS mainly focuses on the gel pores and small capillary pores, and the average porosity by NS is around 4.8%. This result is smaller than those of MIP and NMR, for NS can hardly capture the pore size larger than 50 nm. In addition, the gel pores in NS are much smaller than those in NMR. This verifies that the wetting saturates the C-S-H gels and divides the capillary pores into gel pores [8]. In general, MIP and NMR obtain the largest average porosity of 8.4–9.9%. And they both have a relatively wide measurement range and permit observing most of the porous volume.

In addition, we observe large scattering of porosity among direct methods and among samples of each method (Table 3). This may be because the tested cement paste is manually stripped of concrete in order to remove aggregates but contains uncertain part of aggregates inside. Thus, the presence of aggregates and sampling effects leads to a large variation proportion of cement paste and the porosity of the samples. Meanwhile, the drying/preparing also induces uneven microcracks to the samples, which also contributes to the scattering of pore characterization. Therefore, we mainly focus on the porous volume proportion instead of total porosity due to its scattering, and the following research will be directly applied to prepared cement paste, rather than the extracted cement paste from hardened concrete.

4.2.2. Porosity by Direct Methods. For direct methods, sample imaging has a limit of visual field: the finer the resolution of images, the smaller the area we can observe. XCT has the resolution limit of around 1 μm, and thus, it only permits observing air holes and macrocracks. These porous volumes only occupy a small part of porosity of around 1.8%. In contrast, FIB/SEM can observe capillary pores due to the resolution down to 10 nm, and thus, the porosity observed by FIB/SEM is up to around 16.4%. This result is similar to that of MIP, for both of the methods are focused on the capillary pores (10–1000 nm). However, FIB/SEM is not allowed to observe gel pores due to the resolution of 10 nm. These gel pores are observed in HIM images down to resolution of 1 nm, and they occupy around 0.7–0.9% of porous volume in HIM images. This is in agreement with that by NS of around 0.8%. In total, although FIB/SEM captures the largest porosity of 16.4%, it can only focus on a small range of porous volumes and we can hardly find a method which permits observing all the porous volume. Thus, the pore network characterization by direct methods should be applied by combining the methods in multiscale to contain all the porous volume.

4.2.3. Pore Surface Area. Pore surface area is another parameter to access the porous volume of the material. In Table 3, the pore surface area by multiple methods ranges from 0.001 to 11.637 m^2/g. Despite the measured porosity of 4.8%, NS provides the largest pore surface area of 7.339–11.637 m^2/g. And pore surface area distribution shows the pore surface area is mainly attributed to the micropores in the range of 1–10 nm (Figure 5). In contrast, MIP has a much larger porosity than NS but a much lower pore surface area of around 3.496 m^2/g. This implies that the pore surface area is not only related to the porous volume of the material but also relevant to the fineness of porous volume. The finer the porous volume, the larger the pore surface area. This can be verified by the comparison between pore surface area distribution and pore size distribution by NS (Figures 5(b) and 6(b)).

Similar phenomena are also observed in image analysis. XCT only obtains around 0.001 m^2/g, for it only can observe the isolated air holes and microcracks. Thus, the surface area in such large pores is quite low. FIB/SEM permits observing capillary pores in nanoscale with a relatively high surface area of around 1.846 m^2/g, which is in the same scale but a little smaller than that of MIP.

Meanwhile, we also notice the large variation of pore surface area among samples for each method, which is also due to presence of aggregates and sampling effect.

4.3. Pore Size Distribution. The PSDs of hardened cement paste by multiple methods are presented in Figures 7–12, and the peak sizes of PSDs are listed in Table 4.

4.3.1. Indirect Methods. In Figure 6, the PSD obtained by NS shows similar curves for the three samples, ranging from 2 nm to 70 nm. And the peak size of the three curves all concentrates around 30 nm. This result is in agreement with that of previous literature studies [13, 26]. Although NS can

Table 3: Porosity and pore surface area of hardened cement paste.

Method	Samples	Porosity (%)	Relative volume (%)					Pore surface area (m^2/g)
			Gel pores 1–10 nm	Small capillary pores 10–100 nm	Large capillary pores 0.1–1 μm	Macropores 1–10 μm	Macropores 10–1000 μm	
NS	NS1	3.8	20.8	79.2				7.339
	NS2	5.5	14.1	86.0	—	—	—	11.637
	NS3	5.2	6.9	92.9				10.859
MIP	MIP1	14.8	2.8	69.8	5.1	1.6	6.0	5.368
	MIP2	8.4	0.7	71.0	17.1	2.3	8.7	2.603
	MIP3	4.7	0.0	59.4	15.7	4.5	18.3	0.636
	MIP4	11.8	0.3	77.0	12.5	1.8	8.6	5.378
NMR	NMR1	10.2	48.3	37.4	5.0	4.3	5.1	
	NMR2	6.5	51.1	37.3	4.8	6.8	0.0	
XCT	XCT1	1.8	—	—	—	72.0	28.0	0.001
	XCT2	1.7				68.8	31.2	0.001
FIB/SEM	FS1	16.1	—	78.0	22.0	—	—	1.851
	FS2	16.7		60.8	39.2			1.841
HIM	H1	4.0	0.7	62.7	20.6	—	—	—
	H2	3.4	0.9	53.7	20.0			

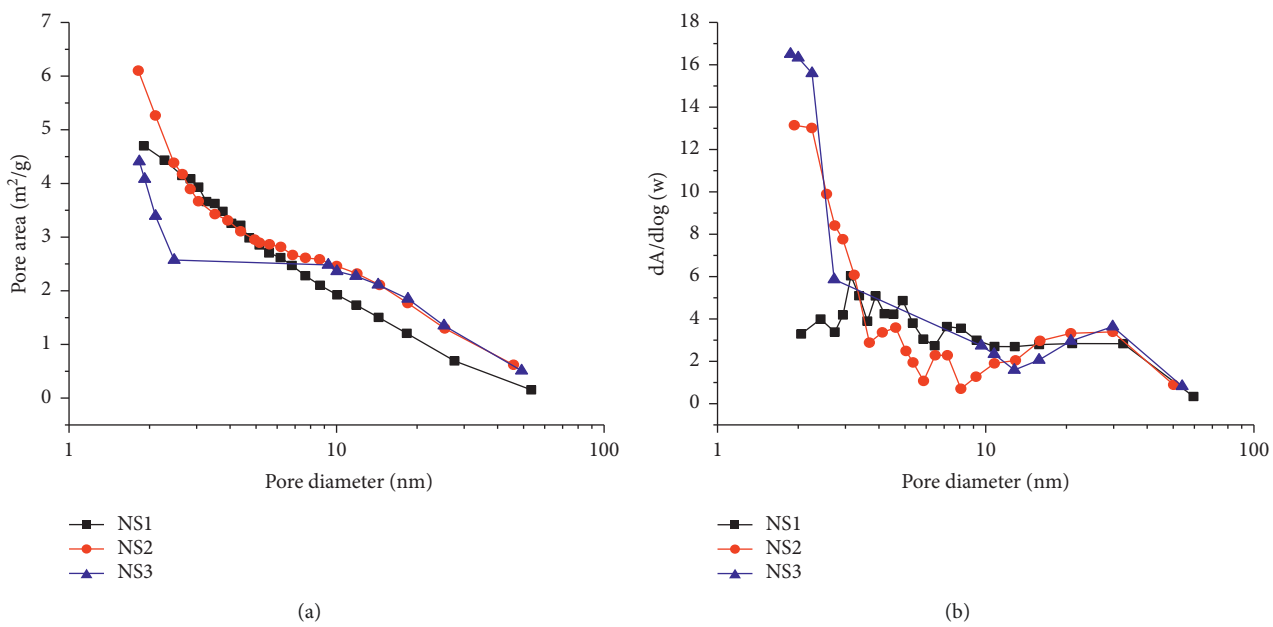

Figure 5: Pore surface area distribution of hardened cement paste by NS: (a) cumulative curve; (b) relative curve.

observe gel pores, the PSD curves show no evident concentration in the range of 0–10 nm. In contrast, the pore surface area distribution by NS is quite different from PSD (Figure 5). It is mainly located in the range of 1–10 nm and only shows small peaks around 30 nm. This verifies that the pore surface area is more related to pore size instead of volume.

In Figure 8, the PSD by MIP is mainly located between 10 and 100 nm. It shows an evident peak of 17 nm and a platform of 40–62 nm. This means that the small capillary pores occupy a large amount of volume in hardened cement paste. Compared with the peak of NS, the largest peak size of 17 nm by MIP is relatively small due to the "ink-bottle" effect [27, 28].

Comparing NS and MIP, the PSDs of NMR show even smaller peak size (around 10 nm) in the range of 10–100 nm (Figure 9). This is because the wetting of cement paste reduces the capillary pore size of cement paste due to swelling of C-S-H gels [8]. In addition, NMR illustrates two large peaks of 300–450 nm and 7–10 μm, which correspond to large capillary pores and air holes/microcracks in hardened cement paste, respectively. These kinds of pores are little influenced by water-induced swelling, and their pore size resides almost constant [8].

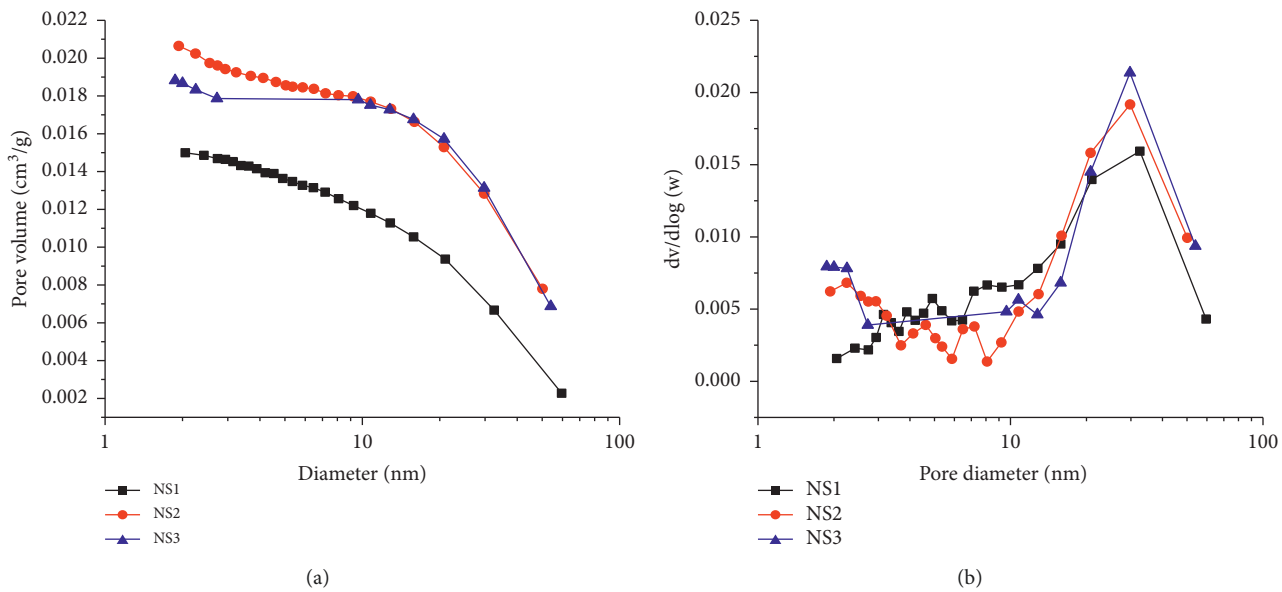

Figure 6: Pore size distribution of hardened cement paste by NS: (a) cumulative curve; (b) relative curve.

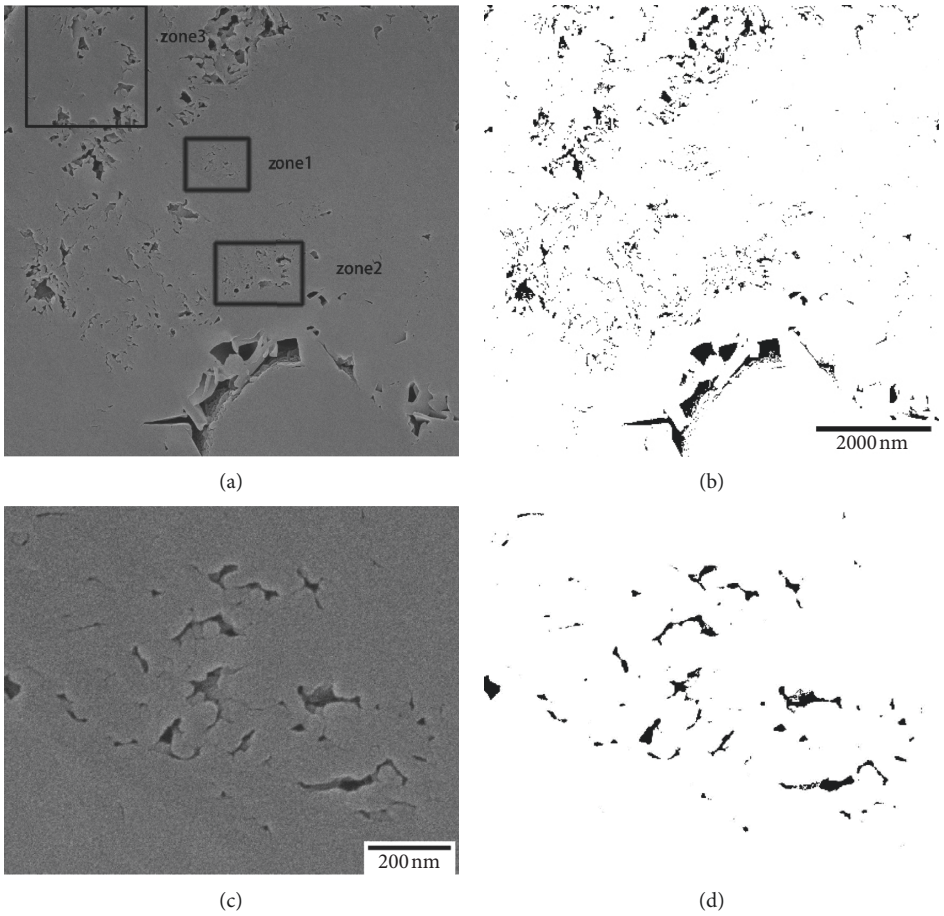

Figure 7: Continued.

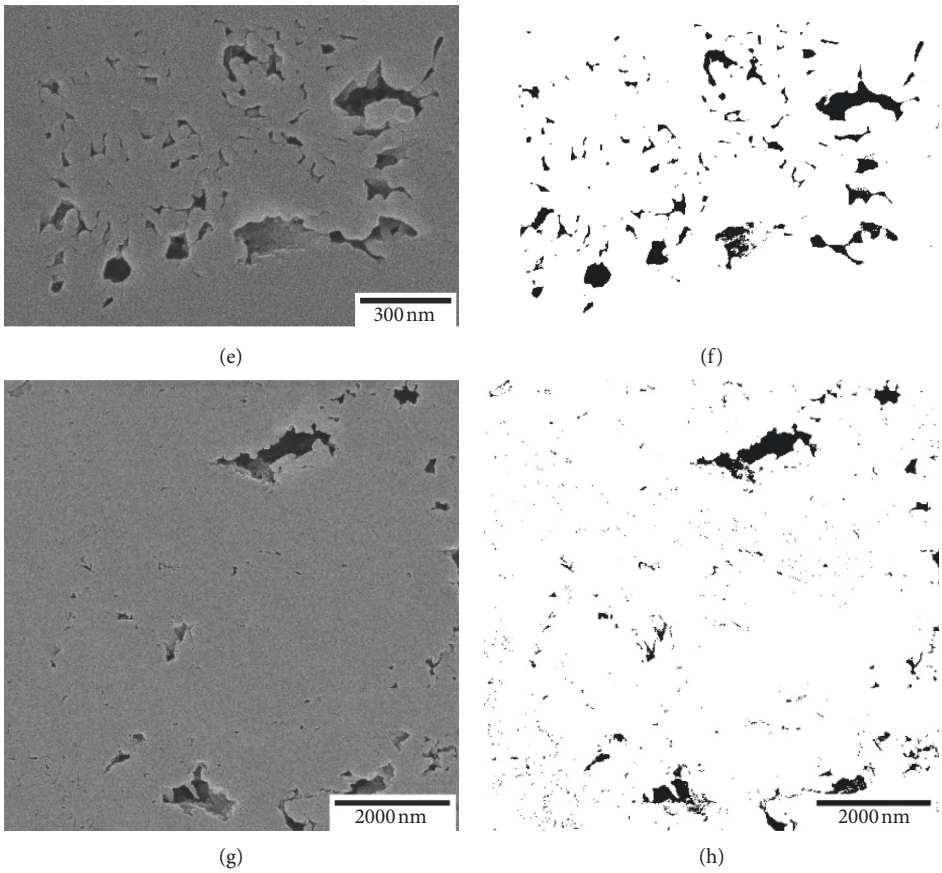

Figure 7: Raw images and segmented porous volume of hardened cement paste by HIM: (a) original images of H1; (b) segmented porous volume of H1; (c) cropped area 1 of H1; (d) segmented cropped zone 1 of H1; (e) cropped zone 2 of H1; (f) segmented cropped area 2 of H1; (g) original images of H2; (h) segmented porous volume of H2.

Table 4: Peak size of porous volume by multiple methods.

Method	Samples	Pore peak size (nm)
Nitrogen sorption	NS1	30
	NS2	30
	NS3	33
MIP	MIP1	17, 40–62
	MIP2	17, 50
	MIP3	17, 40
	MIP4	17, 40
Nuclear magnetic resonance	NMR1	9, 306, 7128
	NMR2	13, 459, 10821
X-ray tomography	XCT1	8000
	XCT2	8000
FIB/SEM	FS1	20, 40, 80
	FS2	20, 40, 80
Helium ion microscopy	H1	8, 12
	H2	8

Unlike porosity, the PSDs of each indirect method all show similar curves and are little influenced by mixing of aggregates. This implies that the sampling effect and presence of aggregates only have large influence on the total porous volume of samples instead of pore size distribution.

4.3.2. Direct Methods. PSDs of two XCT samples show quite similar curves and the same peak size of 8 μm (Figure 10). This peak size is similar to that detected in NMR (7–10 μm), which corresponds to air holes and microcracks in hardened cement paste.

In Figure 11, FIB/SEM focuses on the capillary pores and the two PSD curves show peaks of 20 nm, 40 nm, and 80 nm, which are 2 to 4 times as those of MIP. A similar phenomenon has been also observed in the PSD analysis of COx claystone [20–22]. Since all samples applied to FIB/SEM and MIP are oven-dried at the same temperature, the difference is thus mainly because FIB/SEM measures the porous volume from inner porous volume instead of intruding from the sample surface in MIP [1].

The resolution of HIM images is down to around 1 nm, and their PSDs show the peak of 8–12 nm (Figure 12). This size is quite similar to that of NMR, which proves that HIM can capture gel pores of hardened cement paste.

4.3.3. Influence of Image Resolution. In addition, for direct methods, image resolution is a key factor that may influence the analysis results of porous volume. Hence, we applied HIM to observe two squares of $8^2\,\mu m^2$ with decreasing resolution from 16 nm to 1 nm. As presented in Figure 13, the porous volume is observed more and more

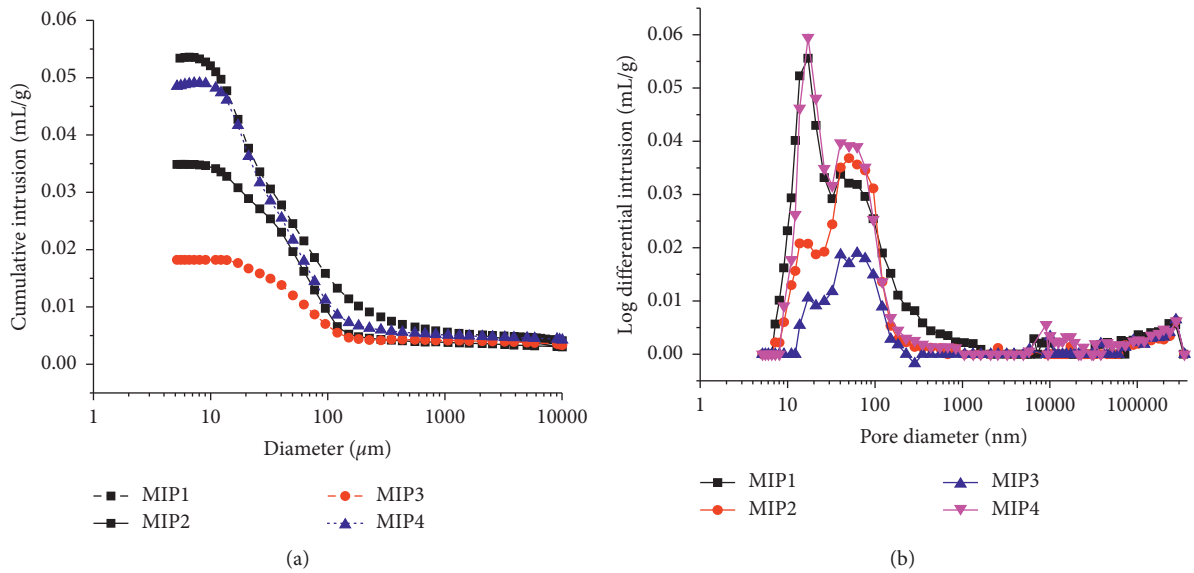

Figure 8: Pore size distribution of hardened cement paste by MIP: (a) cumulative curve; (b) relative curve.

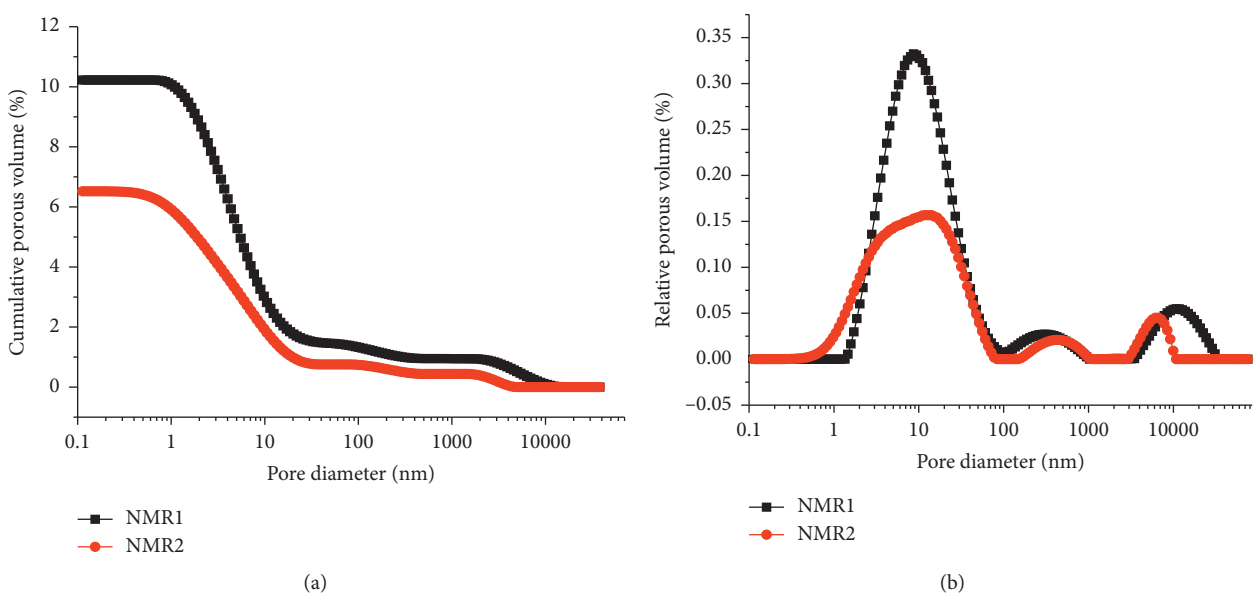

Figure 9: Pore size distribution of hardened cement paste by NMR: (a) cumulative curve; (b) relative curve.

"clearly" with the increasing magnification. Then, we apply the image segmentation and PSD analysis to the images. Figure 14(a) shows that the porosity increases from 2.5% to 4.0% along with the resolution from 16 nm to 1 nm. The increase of porosity mainly lies in the newly observed porous volume, for the cumulative curves are nearly overlapped in the large pore size range. Meanwhile, the variation of image resolution leads to the change of pore size distribution of image analysis (Figure 13(b)), where the peak size changes from 60 nm to 10 nm along with the decreasing image resolution. This indicates that there are more invisible fine pores under the image resolution of FIB/SEM.

4.4. Pore Connectivity. Pore connectivity is also an important parameter for fluid transport, which plays a key role in material transport. It directly decides the transport efficiency of the pore network and is the key parameter in the empirical formula of permeability prediction. The pore connectivity measured by multiple methods is listed in Table 5.

For the indirect methods, NS and MIP are based on material transport in connected volume of materials, and thus, their characterized pore network is all surface-connected volume. In contrast, NMR is only based on the reduction of H in saturated pores and cannot be directly used to detect the pore connectivity of the pore network. However, through mass weighting, the porosity values of NMR1

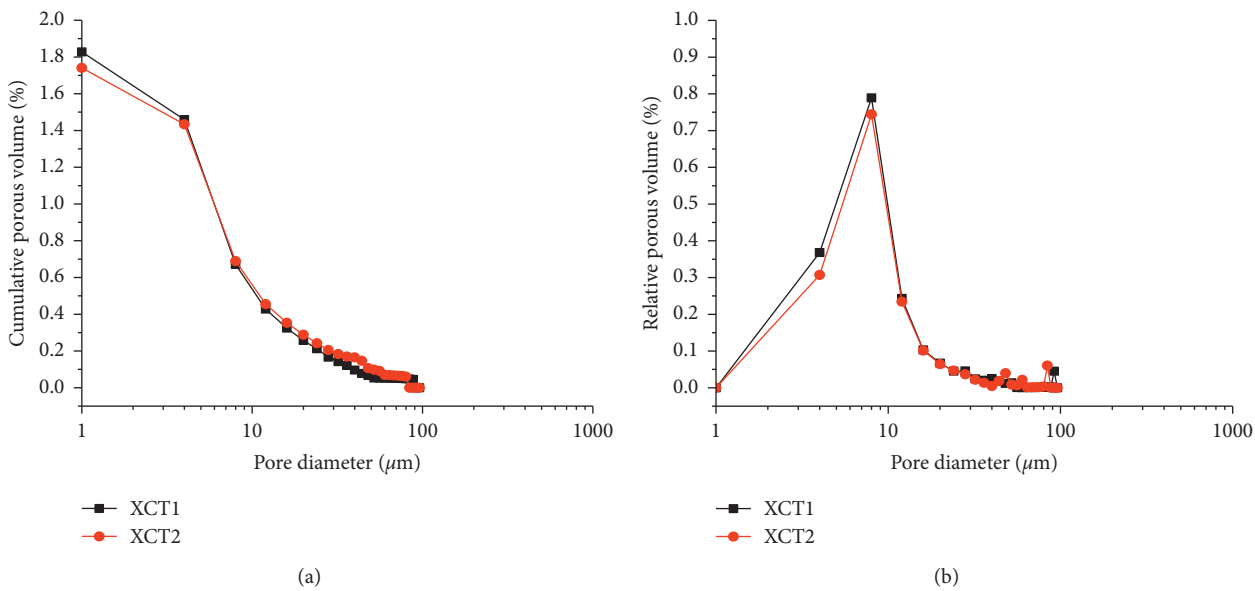

Figure 10: Pore size distribution of hardened cement paste by XCT: (a) cumulative curve; (b) relative curve.

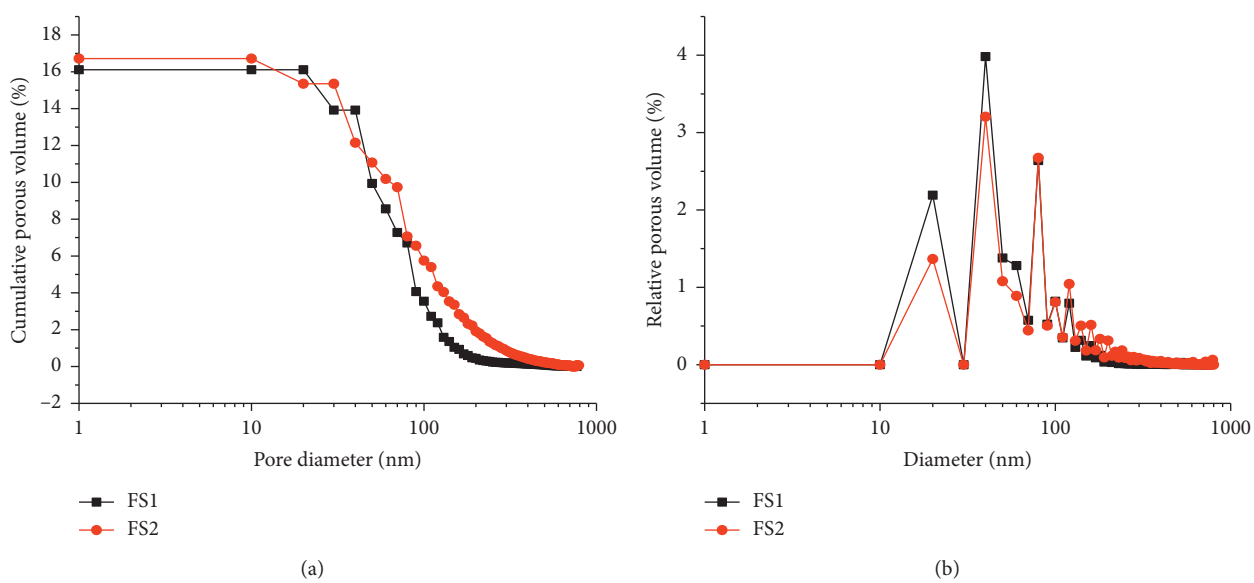

Figure 11: Pore size distribution of hardened cement paste by FIB/SEM: (a) cumulative curve; (b) relative curve.

and NMR2 are measured as 10.8% and 6.5%, respectively, which are similar to and even slightly larger than those of the NMR test (Table 5). This implies that the pore network measured by NMR can be removed outside by oven-drying and thus is also surface-connected. Since the indirect methods permit detecting the porous volume from gel pores to macropores, this proves the universal connectivity of porous volume of hardened cement paste.

As stated above, one single direct method can only capture porous volume in certain scale, and the direct methods permit revealing the connectivity of porous volume in individual scale. For XCT images, the pore network does not show any connectivity (Figure 1), and thus, the connected porosity is 0%. Despite that, theses pores may be partially connected by fine pores without observation of XCT according to the results of MIP and NMR. In Figure 3, the pore network by FIB/SEM is largely surface-connected, which occupies 83.9–84.3% of total porous volume. This proves that the small and large capillary pores observed by FIB/SEM are largely connected. Despite observing finer pores than FIB/SEM, HIM does not show large connectivity in 2D images. This is inconsistent with the result of NS, which shows large porous volume connected by gel pores. This phenomenon may be caused by two reasons: (1) the porous volume in 2D is lack of information for detecting the connectivity of gel pores and (2) there are more porous volumes under observation of HIM (<1 nm). Thus, the direct methods show that the widest connected path of porous volume in hardened cement paste is

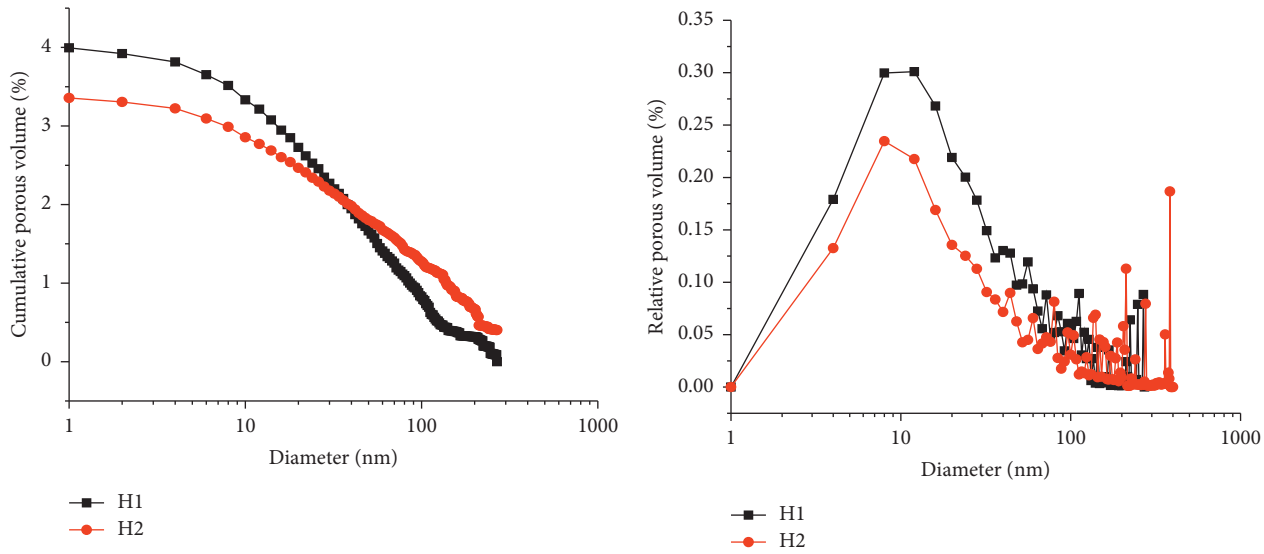

(a) (b)

Figure 12: Pore size distribution of hardened cement paste by HIM: (a) cumulative curve; (b) relative curve.

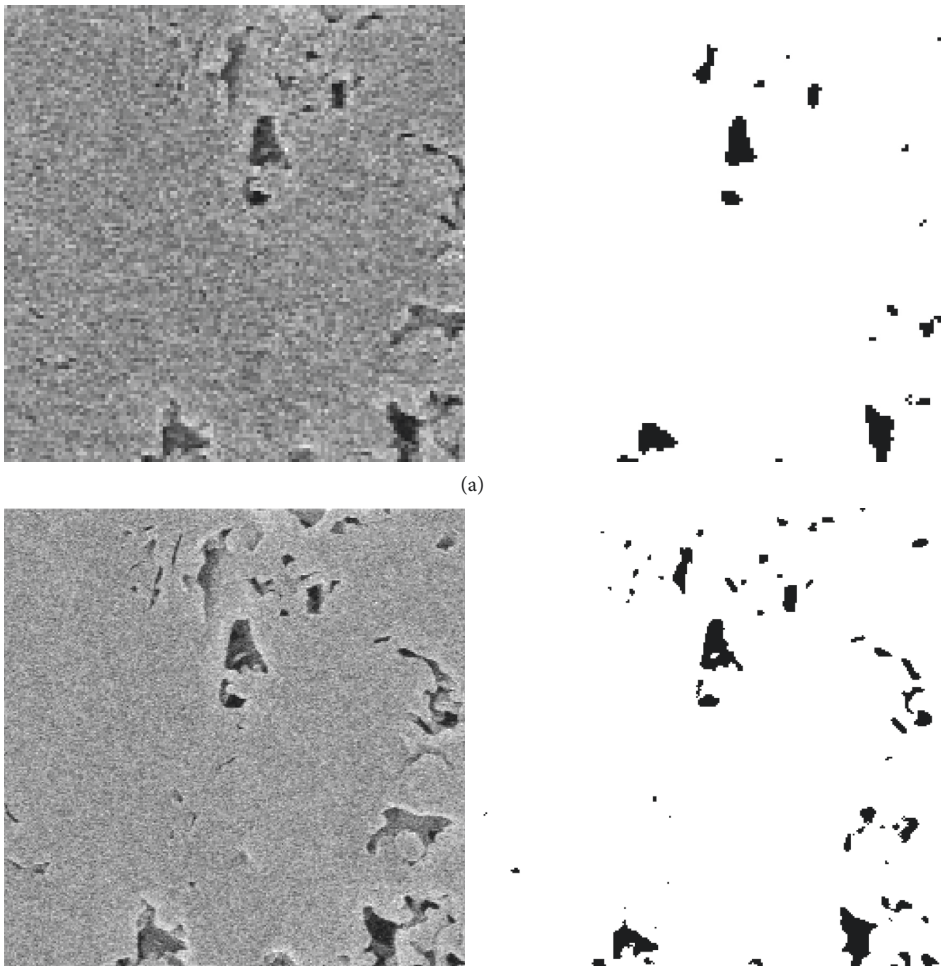

(a)

(b)

Figure 13: Continued.

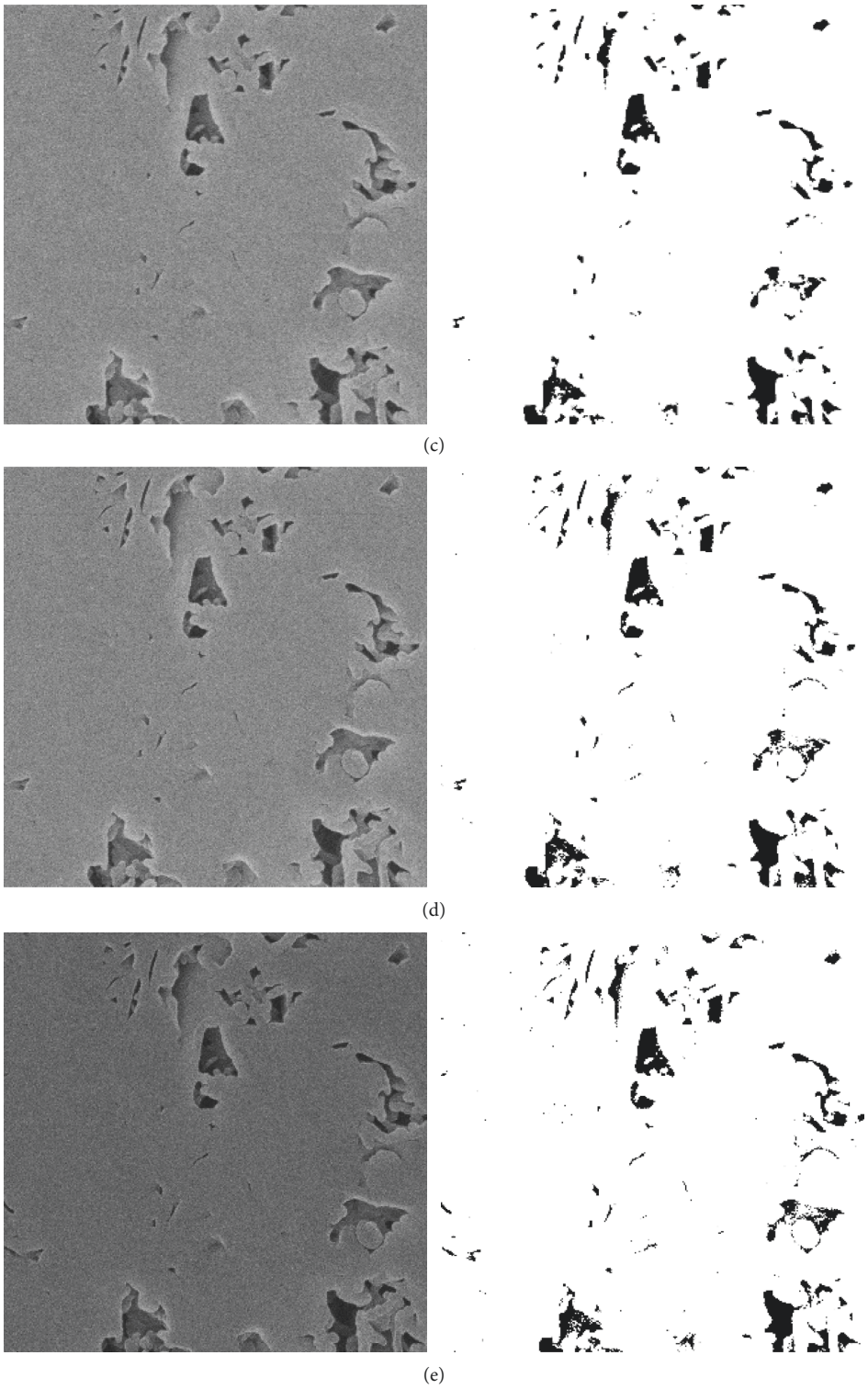

Figure 13: HIM images of zone 3 in H1 with decreasing resolution from 16 nm to 1 nm: (a) resolution of 16 nm; (b) resolution of 8 nm; (c) resolution of 4 nm; (d) resolution of 2 nm; (e) resolution of 1 nm.

the small and large capillary pores, and these pores should be the main passage of mass transport.

4.5. Influence of Microcracks on Porosity, PSD, and Pore Connectivity. In this research, the samples for MIP, NS, XCT, FIB/SEM, and HIM are all oven-dried at 65°C, which ineluctably produces microcracks. However, the indirect methods (MIP and NS) cannot directly detect the microcracks, which instead can be observed by direct methods (XCT and FIB/SEM) (Figure 15). The microcracks in XCT samples are mainly located around aggregates and may

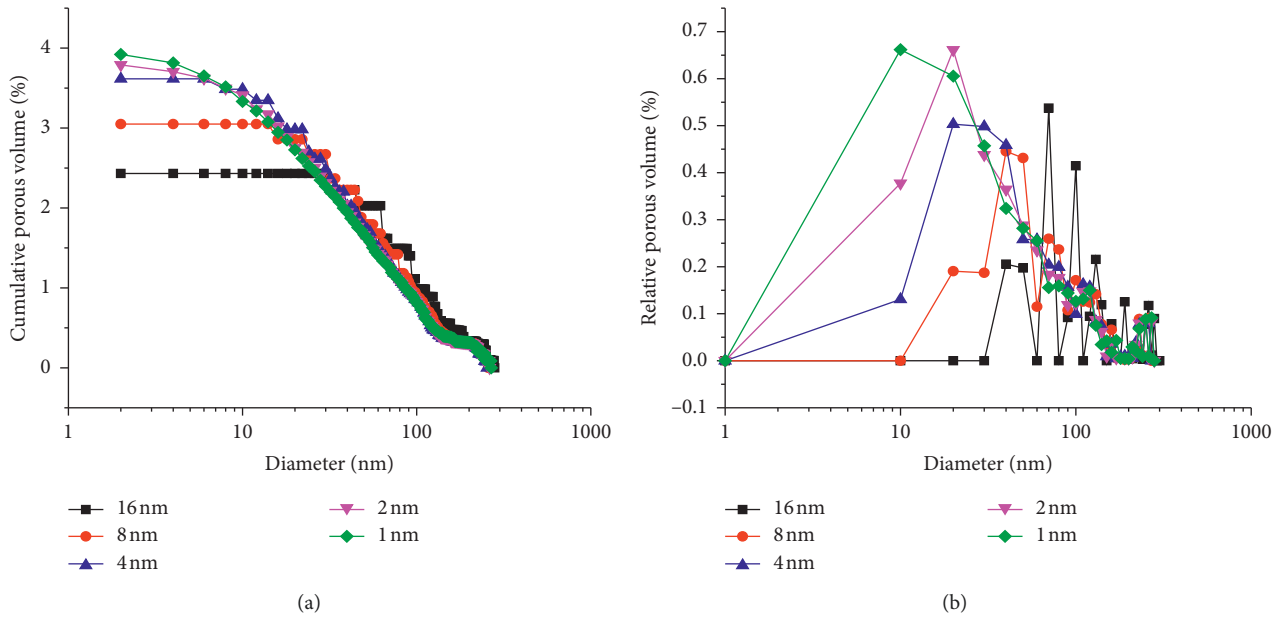

Figure 14: Pore size distribution of HIM images with varying image resolution: (a) cumulative porous volume; (b) relative porous volume.

Table 5: Pore connectivity of porous volume.

Method	Samples	Surface connectivity	Total porosity (%)	Connected porosity (%)
Nitrogen sorption	NS1	Connected	3.8	3.8
	NS2		5.5	5.5
	NS3		5.2	5.2
MIP	MIP1	Connected	14.8	14.8
	MIP2		8.4	8.4
	MIP3		4.7	4.7
	MIP4		11.8	11.8
Nuclear magnetic resonance	NMR1	Not known	10.2	
	NMR2		6.5	
X-ray tomography	XCT1	Not connected	1.8	0
	XCT2		1.7	0
FIB/SEM	FS1	Connected	16.1	13.6
	FS2		16.7	14.0
Helium ion microscopy	H1	Not connected	4.0	0
	H2		3.4	0

generate due to cement paste shrinking during drying. The diameter of microcracks is in the range of 1–10 μm, and this kind of microcrack has also been observed by Wu et al. [29, 30]. The microcracks in XCT only occupy 0.1-0.2% of total porous volume, and thus, little influence of microcracks in macron is induced on the macroporous volume of cement paste. In FIB/SEM images, two parts of microcracks are observed: One part is located around unhydrated paste or aggregates with a smooth surface (Figure 15(a)) and seems to be more isolated. The other part of microcracks is generated around hydrated cement paste, is fully connected with a capillary pore network, and thus may have large influence on the pore network connectivity (Figure 15(b)). Two parts of microcracks occupy 4.5–8.1% of total porous volume and are focused on the diameter of 20–100 nm as original porous volume. The PSDs of microcrack-removed images only show a little variation of the curve form and peak size on the original curves (Figure 16). In addition, the pore connectivity is only slightly weakened after the microcracks of FIB/SEM are removed: the ratio between surface-connected porous volume and total porous volume decreases from 83.0–84.4% to 80.3–82.4%. In total, although the microcracks contribute to total porous volume especially in FIB/SEM images, they have limited influence on the pore size distribution and pore connectivity.

4.6. Representative Property of Testing Samples. Sample mass and volume for all methods are listed in Table 1. For indirect methods, the average sample mass of NS, NMR, and MIP is 0.84 g, 10.23 g, and 1.44 g, respectively. In contrast, the largest sample tested by direct methods is

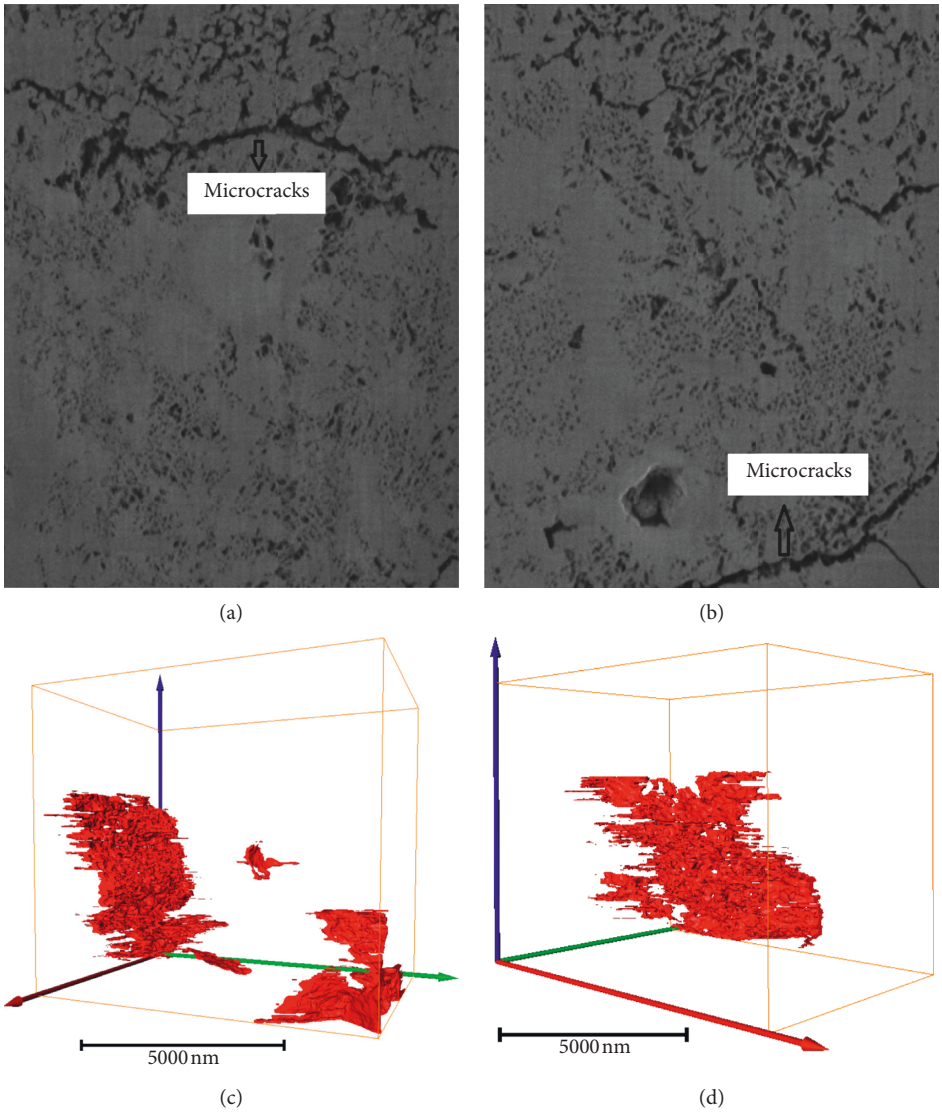

Figure 15: 2D surface and 3D volume of microcracks in FIB/SEM images: (a) microcracks in FS1 with a smooth surface; (b) microcracks in FS1 with a rough surface; (c) microcracks of FS1; (d) microcracks of FS2.

0.0015 g, if the density of hardened cement paste is taken as 2.6 g/cm^3. In other words, the mass of samples applied to indirect methods is at least 560 times as that in direct methods. Therefore, the results of indirect methods should be more representative than those of the direct ones.

In fact, previous literature states that the notion of representative property exists at three scales [31, 32]: a centimetre-sized REV consisting of a mix of aggregates and cement matrix, a REV of the cement matrix (around $100^3\,\mu m^3$ [1]), and a micrometre-sized REV of hydrated foam. The representative property concerned in this research is the second scale (NMR, MIP, NS, and XCT) and third scale (FIB/SEM). Compared to the REV of second scale (around $100^3\,\mu m^3$), the samples for indirect methods (NMR, MIP, and NS) are obviously large enough to be representative, which can be verified by the stability of pore size distribution of samples for each method in Section 4.3. However, the mixing of aggregates in turn leads to a large variation of porosity (Table 3), and therefore, the samples should be up to centimetre-sized (first scale) to be representative. A similar phenomenon has been found for XCT, where samples have a large scale of around 1.0 mm^3 and contain a mix of aggregates. For the other direct methods, the FIB/SEM and HIM are obviously not large enough to be representative of cement aggregates or even the hydrated foam. It can be verified by previous research [1], where a single sample of FIB/SEM is proved to be hardly representative of hydrated cement grains. In total, although the samples in certain methods have a much larger size than $100^3\,\mu m^3$ and stable PSD curves, the mixing of aggregates leads to a large variation of pore characterization, especially the porosity. Thus, the samples tested in this research are not fully representative of hydrated cement paste, and further research will be applied into the prepared hardened cement paste samples.

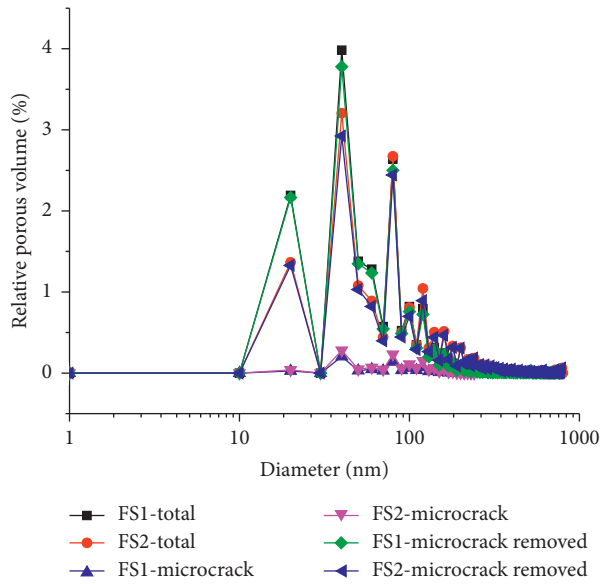

Figure 16: Influence of microcracks on pore size distribution of FIB/SEM samples.

5. Conclusion

To provide a general view of the pore structure of hardened cement paste, we apply indirect methods (NS, MIP, and NMR) and direct methods (XCT, FIB/SEM, and HIM) to characterize the pore network of hardened cement paste from a single concrete of 0.45 W/B ratio. And several conclusions can be summarized as follows.

In 3D view, the pore network is relatively isolated in microscale, whereas the porous volume in nanoscale is largely connected by large capillary pores, small capillary pores, and microcracks. The gel pores in 2D are observed located around capillary pores and seem to be connected with capillary pores in inner volume.

Both MIP and NMR have a wide measurement range and permit observing most of the porous volume of hardened cement paste, obtaining an average porosity of 8.4–9.9%. In contrast, direct methods have a relatively narrow measurement range and thus lead to large porosity scattering of 1.8–16.4%.

The PSD curves by indirect methods show that the pore size of hardened cement paste is mainly concentrated at 1–10 nm, 10–100 nm, and around 10 μm, which correspond to the measurement range of HIM, FIB/SEM, and XCT. However, direct imaging (FIB/SEM) implies that the most porous part of hardened cement paste of 10–100 nm is underestimated by MIP due to the "ink-bottle" effect. The "underestimation" of NMR is due to C-S-H gel swelling during the wetting, which separates the capillary pores into smaller ones.

The microcracks induced by sample preparation contribute 0.1-0.2% (XCT) and 4.5–8.1% (FIB/SEM) of porosity to the porous volume of cement paste, but they have limited influence on the pore size distribution and pore connectivity.

The presence of aggregates and sampling effect leads to large variability of porosity, and thus, the samples tested in this research are not fully representative of hydrated cement paste, and further research will be applied into the prepared hardened cement paste samples.

In total, both direct and indirect methods provide a general view of the pore network of hardened cement paste. The indirect methods have a relatively large measurement scale, but their various assumptions may induce errors in pore characterization. In contrast, direct methods permit observing the images in different scales and provide direct pore characterization. Until now, no imaging method permits observing the gel pores and the macropores at the same time. Thus, the selection of a proper imaging scale and the combination of imaging methods in multiscale will be the main challenge for image analysis.

Data Availability

The data used to support the findings of this study are available from the corresponding author upon request.

Conflicts of Interest

The authors declare that there are no conflicts of interest regarding the publication of this paper.

Acknowledgments

This work was supported by Chinese National Natural Science Foundation (Grant nos. 51708049 and 51678083); Jiangsu Natural Science Foundation Project (Grant no. BK20170293); Open Research Fund of State Key Laboratory of Geomechanics and Geotechnical Engineering, Institute of Rock and Soil Mechanics, Chinese Academy of Sciences (Grant no. Z018020); and Changzhou Science &Technology Program (Grant no. CJ20179043).

References

[1] S. Yang, C. A. Davy, D. Troadec, and X. Bourbon, "Pore network of cement hydrates in a high performance concrete by 3D FIB/SEM—implications for macroscopic fluid transport," *Cement and Concrete Research*, vol. 115, pp. 308–326, 2018.

[2] D. K. Panesar and J. Francis, "Influence of limestone and slag on the pore structure of cement paste based on mercury intrusion porosimetry and water vapour sorption measurements," *Construction and Building Materials*, vol. 52, pp. 52–58, 2014.

[3] M. H. N. Yio, H. S. Wong, and N. R. Buenfeld, "3D pore structure and mass transport properties of blended cementitious materials," *Cement and Concrete Research*, vol. 117, pp. 23–37, 2019.

[4] B. Lu, C. Shi, J. Zhang, and J. Wang, "Effects of carbonated hardened cement paste powder on hydration and microstructure of Portland cement," *Construction and Building Materials*, vol. 186, pp. 699–708, 2018.

[5] M. Wu, K. Fridh, B. Johannesson, and M. Geiker, "Impact of sample crushing on porosity characterization of hardened cement pastes by low temperature calorimetry: comparison of powder and cylinder samples," *Thermochimica Acta*, vol. 665, pp. 11–19, 2018.

[6] Y. Gu, R.-P. Martin, O. Omikrine Metalssi, T. Fen-Chong, and P. Dangla, "Pore size analyses of cement paste exposed to external sulfate attack and delayed ettringite formation," *Cement and Concrete Research*, vol. 123, Article ID 105766, 2019.

[7] A. C. A. Muller and K. L. Scrivener, "A reassessment of mercury intrusion porosimetry by comparison with 1 H NMR relaxometry," *Cement and Concrete Research*, vol. 100, pp. 350–360, 2017.

[8] C. Zhou, F. Ren, Z. Wang, W. Chen, and W. Wang, "Why permeability to water is anomalously lower than that to many other fluids for cement-based material?," *Cement and Concrete Research*, vol. 100, pp. 373–384, 2017.

[9] E. Gallucci, K. Scrivener, A. Groso, M. Stampanoni, and G. Margaritondo, "3D experimental investigation of the microstructure of cement pastes using synchrotron X-ray microtomography (μCT)," *Cement and Concrete Research*, vol. 37, no. 3, pp. 360–368, 2007.

[10] Y. Pei, F. Agostini, and F. Skoczylas, "The effects of high temperature heating on the gas permeability and porosity of a cementitious material," *Cement and Concrete Research*, vol. 95, pp. 141–151, 2017.

[11] M. H. N. Yio, M. J. Mac, H. S. Wong, and N. R. Buenfeld, "3D imaging of cement-based materials at submicron resolution by combining laser scanning confocal microscopy with serial sectioning," *Journal of Microscopy*, vol. 258, no. 2, pp. 151–169, 2015.

[12] K. Lyu, W. She, C. Miao, H. Chang, and Y. Gu, "Quantitative characterization of pore morphology in hardened cement paste via SEM-BSE image analysis," *Construction and Building Materials*, vol. 202, pp. 589–602, 2019.

[13] Y. Zuo and G. Ye, "Pore structure characterization of sodium hydroxide activated slag using mercury intrusion porosimetry, nitrogen adsorption, and image analysis," *Materials*, vol. 11, no. 6, p. 1035, 2018.

[14] S. Lim, H.-S. Lee, and S. Kawashima, "Pore structure refinement of cement paste incorporating nanosilica: study with dual beam scanning electron microscopy/focused ion beam (SEM/FIB)," *Materials Characterization*, vol. 145, pp. 323–328, 2018.

[15] O. Wenzel, M. Schwotzer, E. Müller, V. S. K. Chakravadhanula, T. Scherer, and A. Gerdes, "Investigating the pore structure of the calcium silicate hydrate phase," *Materials Characterization*, vol. 133, pp. 133–137, 2017.

[16] B. Zhou, S. Komulainen, J. Vaara, and V.-V. Telkki, "Characterization of pore structures of hydrated cements and natural shales by 129 Xe NMR spectroscopy," *Microporous and Mesoporous Materials*, vol. 253, pp. 49–54, 2017.

[17] W. Kewen and L. Ning, "Numerical simulation of rock pore-throat structure effects on NMR T_2 distribution," *Applied Geophysics*, vol. 5, no. 2, pp. 86–91, 2008.

[18] P.-S. Liao, T.-S. Chen, and P.-C. Chung, "A fast algorithm for multilevel thresholding," *Journal of Information Science and Engineering*, vol. 17, no. 5, pp. 713–727, 2001.

[19] B. Münch and L. Holzer, "Contradicting geometrical concepts in pore size analysis attained with electron microscopy and mercury intrusion," *Journal of the American Ceramic Society*, vol. 91, no. 12, pp. 4059–4067, 2008.

[20] S. Yang, C. A. Davy, P. Bertier, and D. Troadec, "Understanding fluid transport through claystones from their 3D nanoscopic pore network," *Microporous & Mesoporous Materials*, vol. 228, pp. 64–85, 2016.

[21] S. Yang, C. A. Davy, T. N. Kim et al., "Two-scale analysis of a tight gas sandstone," *Physical Review E*, vol. 94, no. 4, Article ID 043316, 2016.

[22] S. Yang, C. A. Davy, and D. Troadec, "Gas breakthrough pressure (GBP) through claystones: correlation with FIB/SEM imaging of the pore volume," *Oil & Gas Science & Technology*, vol. 71, no. 4, p. 51, 2016.

[23] V. Veligura, G. Hlawacek, R. van Gastel, H. J. W. Zandvliet, and B. Poelsema, "Investigation of ionoluminescence of semiconductor materials using helium ion microscopy," *Journal of Luminescence*, vol. 157, pp. 321–326, 2015.

[24] G. Wegner and E. W. Fischer, "Pure and applied chemistry," *British Medical Journal*, vol. 2, no. 4518, p. 223, 2014.

[25] X. Yang, X. Ke, D. Yang et al., "Effect of ethanol washing of titania clay mineral composites on photocatalysis for phenol decomposition," *Applied Clay Science*, vol. 49, no. 1-2, pp. 44–50, 2010.

[26] J. Kaufmann, "Pore space analysis of cement-based materials by combined Nitrogen sorption—wood's metal impregnation and multi-cycle mercury intrusion," *Cement and Concrete Composites*, vol. 32, no. 7, pp. 514–522, 2010.

[27] B. Li, J. Mao, T. Nawa, and T. Han, "Mesoscopic damage model of concrete subjected to freeze-thaw cycles using mercury intrusion porosimetry and differential scanning calorimetry (MIP-DSC)," *Construction and Building Materials*, vol. 147, pp. 79–90, 2017.

[28] J. Tatar, N. R. Brenkus, G. Subhash, C. R. Taylor, and H. R. Hamilton, "Characterization of adhesive interphase between epoxy and cement paste via Raman spectroscopy and mercury intrusion porosimetry," *Cement and Concrete Composites*, vol. 88, pp. 187–199, 2018.

[29] Z. Wu, N. R. Wong, and N. R. Buenfeld, "Influence of drying-induced microcracking and related size effects on mass transport properties of concrete," *Cement and Concrete Research*, vol. 68, pp. 35–48, 2015.

[30] Z. Wu, H. S. Wong, and N. R. Buenfeld, "Transport properties of concrete after drying-wetting regimes to elucidate the effects of moisture content, hysteresis and microcracking," *Cement and Concrete Research*, vol. 98, pp. 136–154, 2017.

[31] M. H. N. Yio, H. S. Wong, and N. R. Buenfeld, "Representative elementary volume (REV) of cementitious materials from three-dimensional pore structure analysis," *Cement and Concrete Research*, vol. 102, pp. 187–202, 2017.

[32] M. Königsberger, M. Hlobil, B. Delsaute, S. Staquet, C. Hellmich, and B. Pichler, "Hydrate failure in ITZ governs concrete strength: a micro-to-macro validated engineering mechanics model," *Cement and Concrete Research*, vol. 103, pp. 77–94, 2018.